Sensors and Materials, Vol. 37, No. 12 (2025) 5789–5804
MYU Tokyo

S & M 4279

Design Optimization of Dual-outlet Blower Motor Using Finite Element and Taguchi Methods for Air-conditioning Applications

Chun-Chieh Chang,[1] Zhi-Hong Lin,[2] Chao-Ming Hsu,[2]
Fu-Ming Chen,[3] Bo-Wun Huang,[3] and Cheng-Yi Chen[1*]

[1]Department of Electrical Engineering, Cheng Shiu University, Kaohsiung 833, Taiwan
[2]Department of Mechanical Engineering, National Kaohsiung University of Science and Technology, Kaohsiung 807, Taiwan
[3]Institute of Mechatronic Engineering, Cheng-Shiu University Kaohsiung City 833, Taiwan

(Received November 23, 2025; accepted December 19, 2025)

Keywords: dual-outlet blower motor, air conditioning system, Taguchi method, sensitivity analysis

In this study, we present the design and optimization of a compact dual-outlet blower motor developed for commercial vehicle air-conditioning systems. The proposed motor was engineered to meet stringent performance requirements across both low- and high-speed operating ranges. The initial motor geometry was modeled and analyzed using Altair FluxMotor, after which Altair Flux2D was employed for mesh generation, circuit configuration, and detailed electromagnetic performance evaluation, including torque ripple, back electromotive force (back-EMF), efficiency, and line-to-line voltage. A comparative assessment of multiple slot/pole configurations identified the 8-pole/12-slot topology as the most suitable design. Sensitivity analysis revealed that slot opening width, air gap, magnet thickness, magnet arc angle, number of turns, and wire diameter are the dominant parameters affecting overall motor behavior. To achieve systematic and efficient optimization, the Taguchi method was applied. Simulation results showed that, at an input current of 1.35 A and a speed of 2678.5 rpm, the motor efficiency improved from 67 to 82%. Under a constant line-to-line voltage of 21 V, the speed increased from 2678 to 3178 rpm, efficiency rose from 67 to 74.1%, and torque ripple was markedly reduced from 114 to 22.2%. Furthermore, the fabricated prototype and experimental validation confirmed close agreement with the simulation outcomes. These results demonstrated the effectiveness of the proposed optimization methodology and highlighted its applicability to developing compact, high-efficiency blower motors for modern vehicle air-conditioning systems.

1. Introduction

Blower motors are widely used in heating, ventilation, and air-conditioning (HVAC) systems to maintain a comfortable temperature across varying ambient conditions, where high-speed operation is often required to adjust cabin temperature rapidly. However, electromagnetic interaction between the rotor and stator generates cogging torque at low speeds and torque ripple at high speeds, causing vibration, noise, and efficiency loss. Thus, smooth torque delivery and

*Corresponding author: e-mail: k0464@gcloud.csu.edu.tw
https://doi.org/10.18494/SAM6076

ISSN 0914-4935
https://myukk.org/

optimized electromagnetic design are key research priorities. To address this issue, an asymmetric rotor pole design was proposed to suppress torque ripple.[1] A comparative evaluation of brushless direct current (BLDC) motor configurations (4-pole/9-slot, 4-pole/15-slot, and 4-pole/18-slot) identified the 4-pole/15-slot arrangement as the most effective for minimizing torque ripple.[2] On the basis of this configuration, further refinement of magnet type, rotor geometry, and stator slot opening width was applied to improve performance. Maxwell 2D finite-element simulations were used in related optimization studies, and magnet spacing, rotor air gap, and stator geometry were shown to significantly influence torque ripple reduction.[3,4] Additional research on 8-pole motors showed that the 8-pole/60-slot design delivers the highest output torque with relatively low detent torque when geometric modifications are applied.[5] Optimization of key stator parameters using the Taguchi method, followed by one-factor convergence analysis, further demonstrated that slot geometry—particularly slot opening width—substantially affects cogging torque and back electromotive force (back-EMF) performance, yielding a moderate speed improvement (~100 rpm).[6]

Optimization of magnet dimensions, air gap, and magnet arrangement patterns has been shown to improve magnetic field uniformity and torque characteristics, considering both stator structural design and rotor-related parameters.[7] Torque-harmonic amplitude variation under different magnet placement distances was evaluated in a synchronous reluctance motor rotor, and an analysis of rotor–stator configuration interaction yielded an optimized rotor design with reduced torque ripple.[8] In fan applications, a BLDC motor designed using three-dimensional finite element analysis (FEA) demonstrated that integrating V-shaped and inclined permanent magnets can reduce both cogging torque and axial force components by approximately 50% while maintaining magnetic balance.[9] For ceiling fan applications, an 8-pole/24-slot motor underwent parametric optimization of slot opening width, magnet arc angle, and air gap, followed by experimental validation confirming improved efficiency.[10] Additionally, a rotor design using elastic permanent magnets was analyzed through FEA, and geometric deformation and air gap characteristics were shown to significantly affect magnetic reluctance and flux distribution.[11]

Beyond simulation-based studies, the Taguchi method has been widely adopted for motor optimization. It enables the systematic identification of influential factors through orthogonal array and analysis of variance (ANOVA) analysis, producing designs that effectively meet performance objectives.[12] In motor applications, the Taguchi method has been applied to enhance power density and reduce noise, improve energy efficiency in ceiling fan motors with different pole–slot ratios, and optimize the magnet arrangement and spacing for jet impeller BLDC motors.[13,14] Furthermore, the simultaneous optimization of stator outer diameter, magnet dimensions, pole-arc coefficient, and air gap has been shown to improve rated torque and efficiency and reduce core losses while maintaining magnetic flux balance.[15] Overall, the literature confirms that the geometric optimization of both the rotor and the stator, combined with statistical design techniques such as the Taguchi method, can significantly enhance torque performance, reduce torque ripple and back-EMF distortion, and improve overall efficiency.

Building upon an automotive blower motor as the foundation of this study, the primary objective is to extend its applicability to vehicle HVAC systems through enhanced

electromagnetic and structural design. In practical operation, blower motors typically run at approximately 1000–3000 rpm. At such speeds, cogging torque often leads to uneven rotation. In contrast, at higher speeds, torque ripple induces mechanical vibration and acoustic noise—both of which degrade passenger comfort and system efficiency. To overcome these limitations, in this paper, we propose a comprehensive design strategy to achieve low cogging torque, low torque ripple, and reduced back-EMF, thereby facilitating higher operational speeds. A comparative performance evaluation is first conducted among four different slot/pole combinations and various winding configurations of BLDC motors to identify the configuration with optimal performance characteristics. The most favorable motor design is then further refined by the Taguchi optimization method, focusing on critical design parameters such as stator slot geometry, rotor dimensions, and winding specifications. Through this systematic optimization process, the proposed approach seeks to improve the efficiency, stability, and reliability of the blower motor while simultaneously reducing vibration, noise, and maintenance requirements.

2. Motor Design and Simulation Analysis

The motor selected for this study is a dual-outlet blower motor (model B080D024-001), commonly used in automotive air conditioning systems.[16] Its external appearance is shown in Fig. 1, and the corresponding specifications are summarized in Table 1. The motor operates at a rated input voltage of 24 V and an input current of 6.5 A, delivering a maximum speed of 3750 rpm. The stator geometry features an outer diameter of 70 mm, an inner diameter of 35 mm, and a thickness of 20.6 mm.

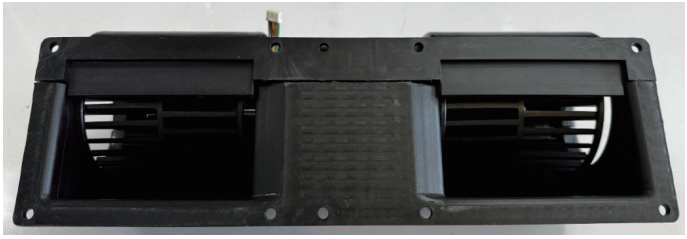

Fig. 1. (Color online) Double air outlet blower appearance.[16]

Table 1
Motor specifications.

Description	Quantity	Unit
Number of poles	4	pole
Number of slots	12	slot
Rated speed	3750	rpm
Stator outer diameter	70	mm
Stator inner diameter	35	mm
Rotor outer diameter	34.24	mm
Rotor inner diameter	7.96	mm
Number of turns	50	turns

2.1 Motor design simulation analysis

In this study, Altair FluxMotor and Flux software were used for motor design, modeling, and analysis. The blower motor uses a 4-pole/12-slot distributed winding configuration, as shown in Fig. 2, with simulation conditions summarized in Table 2. The permanent magnets are radially magnetized, and the windings consist of 0.4 mm enameled wire with 50 turns per coil arranged in a Y-connection. The stator core is composed of 41 silicon steel laminations, each with a thickness of 0.5 mm, resulting in a total stator stack length of 20.5 mm. This thickness is slightly smaller than the original design specification of 20.6 mm, thereby ensuring compatibility with the existing product casing and allowing direct assembly without mechanical modification. Under the 120° conduction mode, a comparison between the simulation and experimental results presented in Table 3 indicates discrepancies in both current and voltage, which are primarily attributed to slight differences between the modeled and actual winding resistance. To further examine this deviation, a no-load back-EMF test was performed, as shown in Fig. 3. The measured peak back-EMF voltage was 15.6 V, whereas the simulated value was 13 V. This difference is mainly due to nonuniform winding distribution and environmental variations during experimental testing.

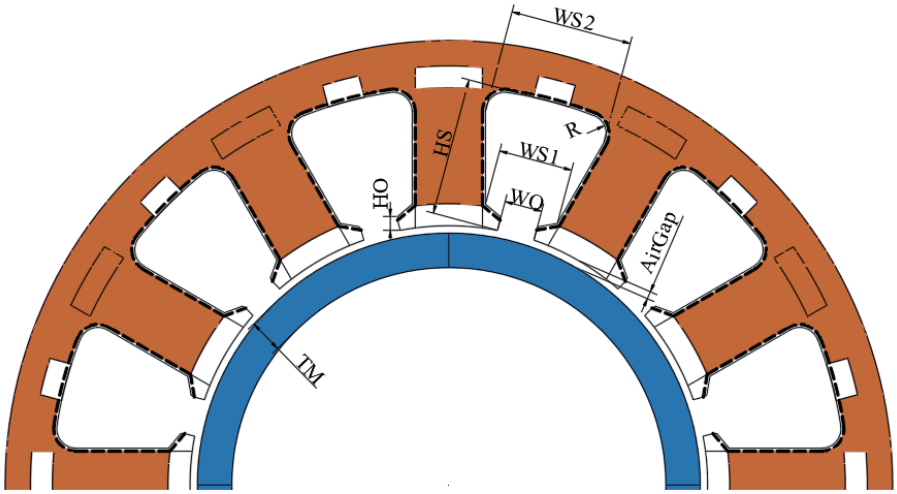

Fig. 2. (Color online) Motor geometry.

Table 2
Initial stator symbol size specifications.

Description	Size (mm)
Slot height (HS)	9.3
Height of slot opening (HO)	1.0
Width of slot opening (WO)	2.55
Intermediary width of the slot (WS1)	4.8
Slot width (WS2)	8.7
Top slot radius (R1)	1.5
Air gap	0.38
Magnet thickness (TM)	2.4

Table 3
Measured vs simulated results for the 4-pole/12-slot distributed winding motor.

Item	Current (A)	Line voltage (V)	Speed (rpm)	E. power (W)	M. power (W)	Torque (N·m)	Efficiency (%)
Measured	1.67	17.51	2678.5	44.9	30.85	0.11	68.7
Simulated	1.35	21.48	2678.5	44.8	30.03	0.11	67.0

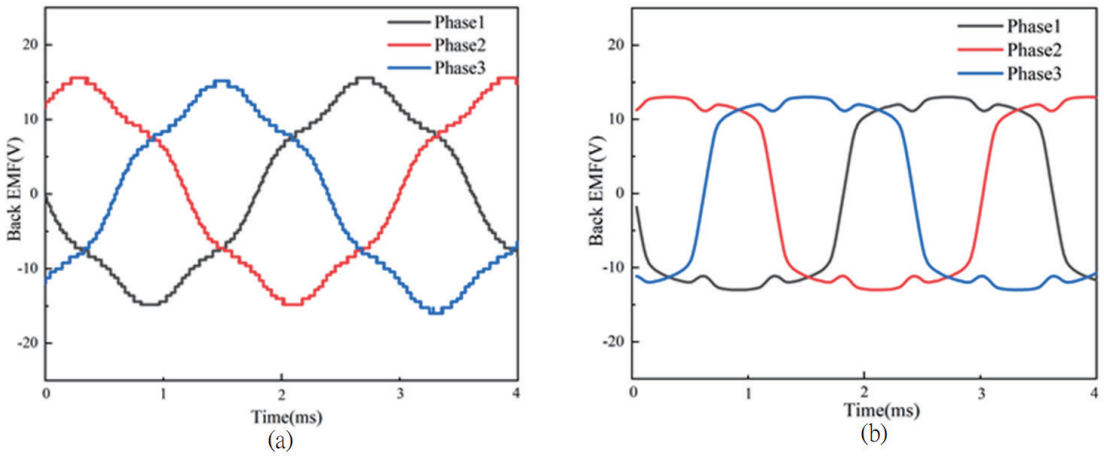

Fig. 3. (Color online) Back-EMF waveforms: (a) experimental measurement and (b) simulation.

2.2 Comparison of motor designs with different slot-to-pole combinations

The slot-to-pole combination of a motor directly affects its rotational speed and torque characteristics. As the number of poles increases, the motor generally produces higher torque, but this often comes at the expense of maximum speed. Therefore, when designing the pole configuration, it is essential to carefully evaluate factors such as the intended operating range, maximum torque requirement, and overall cost to ensure optimal performance. To reduce torque ripple, the cogging torque must first be minimized, which can be achieved by selecting the slot-to-pole combination appropriately. A commonly used evaluation coefficient for analyzing slot-to-pole combinations is expressed as[17]

$$C_t = \frac{N_p \times N_s}{N_c}, \tag{1}$$

where C_t denotes the combination coefficient, N_p represents the number of poles, N_s is the number of slots, and N_c refers to the least common multiple of the slot and pole numbers. This formula is primarily used to analyze the relationship between the number of slots (N_s) and the number of poles (N_p), which serve as indicators of magnetic field periodicity and winding symmetry. It is commonly applied in the design and analysis of BLDC and permanent magnet synchronous motors. The results for various slot–pole combinations based on a 4-pole/12-slot reference motor are summarized in Table 4. As observed, when N_s and N_p share a larger common

Table 4
Different slot-to-pole combinations.

N_s	N_p	N_c	C_t	N_s	N_p	N_c	C_t
3	2	6	1	9	6	18	3
3	4	12	1	9	8	72	1
6	2	6	2	12	2	12	2
6	4	12	2	12	4	12	4
9	2	18	1	12	8	24	4
9	4	36	1	12	10	60	2

divisor, the C_t value increases, indicating a higher cogging torque frequency and consequently lower torque ripple. Conversely, when N_s and N_p are nearly coprime, the C_t value decreases, which tends to result in greater cogging torque fluctuation.

In this study, several slot-to-pole configurations were compared to assess their impact on motor performance. Specifically, four designs were analyzed: a 4-pole/12-slot concentrated winding (CW), a 4-pole/12-slot distributed winding (DW), a 4-pole/6-slot CW, and an 8-pole/12-slot CW. Using the 4-pole/12-slot DW motor operating at an input current of 1.35 A and a speed of 2678.5 rpm as a reference, we performed simulation analyses to compare torque, efficiency, and other key performance parameters. The results, summarized in Table 5, reveal that the 8-pole/12-slot motor achieved the highest efficiency and output torque among the tested configurations. Consequently, this slot-to-pole combination was selected for subsequent optimization. Although its torque ripple was initially higher, further refinement and optimization are expected to reduce this effect and enhance the overall performance of the motor.

3. Optimization Design of BLDC Motor

In this study, we aim to reduce torque ripple and back-EMF to enhance the stability and rotational speed of the motor. We focused on an 8-pole/12-slot CW BLDC motor; its initial design specifications are listed in Table 2. A sensitivity analysis approach was adopted to investigate the key design factors that significantly affect cogging torque, torque ripple, and back-EMF, as identified in previous studies. During the simulation process, only one parameter was varied at a time. At the same time, all other conditions were kept constant, to observe the effects of dimensional changes on back-EMF, torque ripple, output torque, and efficiency. On the basis of the results of this analysis, the most influential control factors were identified and subsequently used as the basis for the Taguchi optimization design.

3.1 Sensitivity analysis

According to the related literature, several key design factors have been identified as having a significant impact on motor performance.[17–21] These include magnet thickness, slot depth, shoe height, slot opening width, air gap, and magnet expansion angle. In this study, a sensitivity analysis was conducted on these six factors. During the simulation, only one parameter was varied at a time. To achieve the dual objectives of increasing motor speed and reducing line-

Table 5
Motor performances of different slot-to-pole configurations.

Motor configuration	Torque (N·m)	Torque ripple (%)	Electrical power (W)	Mechanical power (W)	Efficiency (%)
4-pole/12-slot CW	0.06	164.2	27.1	15.81	58.3
4-pole/12-slot DW	0.11	114.01	44.8	30.03	67.0
4-pole/6-slot CW	0.12	99.14	44.1	32.61	73.9
8-pole/12-slot CW	0.21	109.09	75.82	58.63	77.3

voltage requirements, we also investigated the effect of winding resistance by varying the wire diameter. On the basis of commonly used industrial wire specifications, three larger diameters—0.5, 0.55, and 0.6 mm—were selected to replace the original 0.4 mm wire. These were incorporated as control factor levels in the subsequent Taguchi optimization design.

Considering the manufacturability of commercially available magnets, the minimum feasible magnet thickness is approximately 1 mm. Therefore, we adopted 2.4 mm as the baseline design dimension and varied the thickness in 0.2 mm increments for the sensitivity analysis, observing how dimensional changes affect performance parameters, as illustrated in Fig. 4(a). The results show that as the magnet thickness increases, the torque ripple remains relatively unchanged, whereas the back-EMF, output torque, and efficiency initially increase and then stabilize. Since the objective of this research is to reduce back-EMF, three thickness values—1.2, 1.4, and 1.6 mm—were selected as the design parameters for subsequent simulation analysis.

When modifying the slot depth, the slot fill factor must also be considered, as increasing the slot depth generally results in a lower fill factor. In this study, a baseline slot depth of 9.3 mm was selected, and the parameter was varied in 0.5 mm increments to examine the effect of dimensional changes on the target performance metrics, as shown in Fig. 4(b). The results indicate that variations in slot depth have no significant effect on torque ripple, efficiency, output torque, or back-EMF. Therefore, the slot depth was fixed at the initial design value of 9.3 mm for subsequent analyses.

When adjusting the slot-opening width, the limitations imposed by the conductor diameter and the winding-nozzle size must be considered. An excessively narrow opening markedly increases the difficulty of winding. In this study, a larger wire diameter was adopted to reduce the number of turns—and thereby the back-EMF—while maintaining the required current capacity. Consistent with manufacturability constraints reported for nozzle-wound CW, the minimum slot-opening width is governed by the wire diameter and the nozzle wall thickness.[21] For the proposed process, a threshold of 1.96 mm was identified to enable smooth insertion without damaging the wire or causing feeding difficulties. Accordingly, a central design value of 2.55 mm was selected, and parametric simulations were performed in 0.2 mm increments to evaluate the effect of slot opening width on performance, as illustrated in Fig. 4(c). The results indicate that increasing the slot opening width leads to decreases in back-EMF, efficiency, and output torque, while torque ripple increases. At 1.96 mm, torque ripple attains its minimum and both efficiency and torque are favorable; however, the back-EMF remains relatively high, which may adversely affect control stability. These observations motivate further multi-parameter optimization to achieve a balanced design.

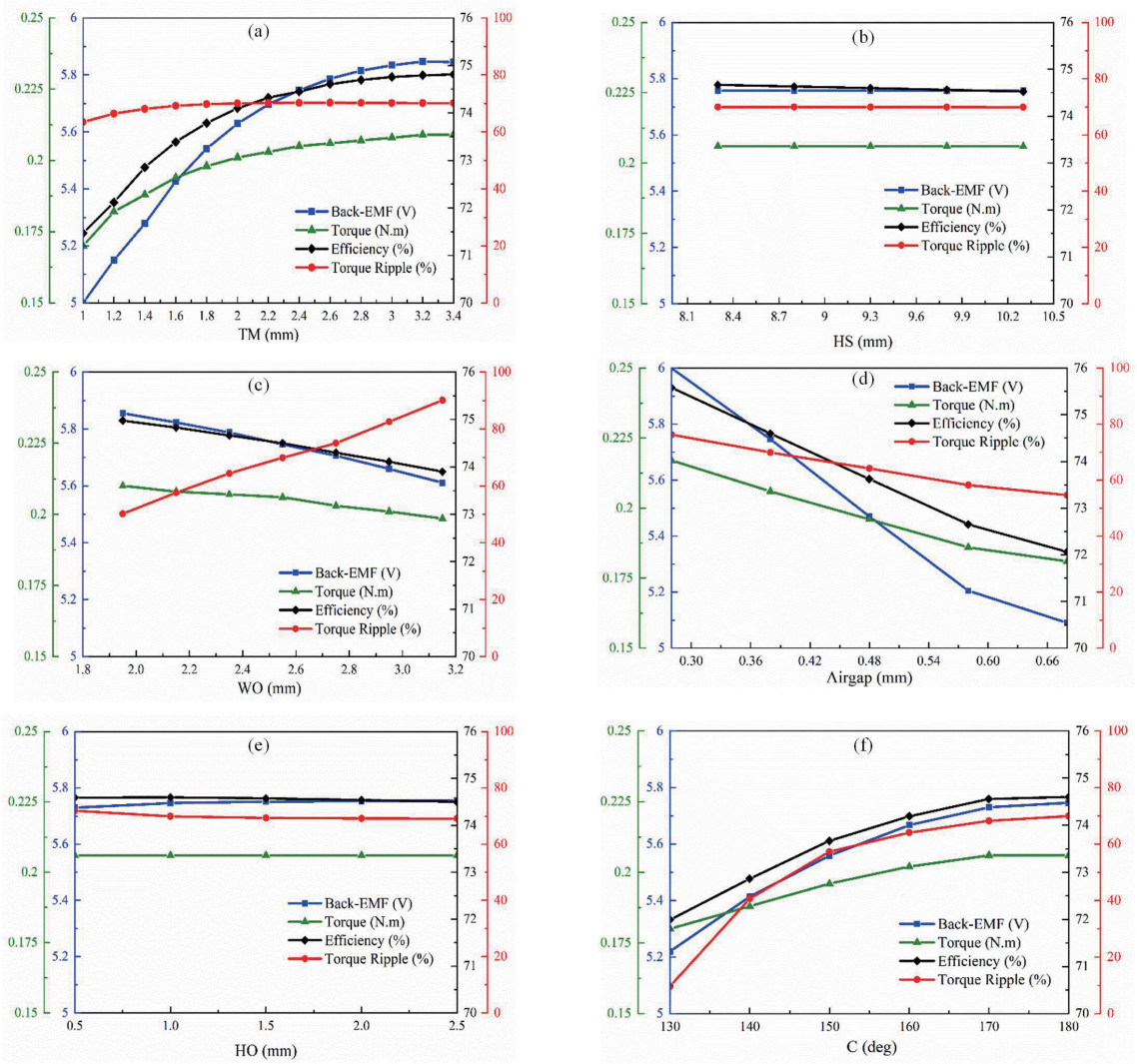

Fig. 4. (Color online) Sensitivity analysis: (a) magnet thickness, (b) slot depth, (c) slot opening width, (d) air gap, (e) stator shoe height, and (f) magnet expansion angle.

The air gap has a significant impact on the performance of both the stator and rotor in a motor. A large air gap leads to reduced efficiency, whereas an overly small air gap increases manufacturing difficulty. From the design experience with commercial fan motors, the typical air gap is approximately 0.5 mm. In this study, a baseline air gap of 0.38 mm was adopted, and simulations were performed at 0.1 mm intervals to evaluate how air gap variations affect performance characteristics, as illustrated in Fig. 4(d). The results indicate that as the air gap increases, the back-EMF, output torque, efficiency, and torque ripple all show a clear downward trend. When the air gap is 0.28 mm, both efficiency and output torque reach their maximum values, but the back-EMF and torque ripple become relatively large. Conversely, at 0.68 mm, efficiency and output torque drop significantly, making this configuration unsuitable. Therefore, considering both performance and manufacturability, we selected 0.38, 0.48, and 0.58 mm as the air gap levels for the subsequent Taguchi optimization design.

The stator shoe height must be carefully selected, considering both manufacturing feasibility and its impact on the winding process. If the height is too low, it may cause structural damage during machining, whereas an excessive height can increase winding difficulty. In this study, a baseline stator shoe height of 1.0 mm was chosen, and the parameter was varied in 0.5 mm increments to evaluate its impact on motor performance, as shown in Fig. 4(e). The results indicate that changes in shoe height have no significant effect on back-EMF, output torque, efficiency, or torque ripple. Therefore, the stator shoe height was fixed at the initial design value of 1.0 mm for all subsequent analyses.

To reduce magnet usage and thereby lower manufacturing costs, we adopted a magnet expansion angle of 180° as the baseline design and decreased it in 10° intervals to evaluate the effects of different angles on back-EMF, torque ripple, torque, and efficiency. As illustrated in Fig. 4(f), all performance indicators exhibit an increasing trend as the magnet arc angle increases. However, since the primary objective of this study is to reduce torque ripple and back-EMF, three magnet expansion angles—130, 140, and 150°—were selected as the design levels for the subsequent Taguchi optimization, aiming to achieve a balance between performance improvement and material cost reduction.

The results of the sensitivity analysis identified six key design factors—magnet thickness, slot opening width, air gap, magnet expansion angle, wire diameter, and number of winding turns—that have a significant impact on torque ripple, back-EMF, and efficiency. These parameters were selected as control factors for the subsequent Taguchi optimization design, which systematically investigates their effects on motor performance through level configuration and orthogonal array analysis. This approach reduces the number of required simulations while allowing the evaluation of both main and interaction effects. The optimization aims to achieve three main objectives: (1) reduce torque ripple and back-EMF to improve operational stability and minimize vibration and noise at different speeds, (2) enhance energy conversion efficiency under constant input and rotational conditions, and (3) balance performance improvement with material and manufacturing cost reduction, particularly by optimizing magnet geometry to minimize magnet usage. Through this method, we established an optimal design parameter combination that ensures both high performance and cost effectiveness, providing a practical foundation for future motor development.

3.2 Taguchi-based optimization process and its outcomes

On the basis of the results of the sensitivity analysis, the primary design factors that significantly affect motor performance, along with their corresponding level settings, are summarized in Table 6. To perform parameter optimization, we employed an L27 orthogonal array in accordance with the Taguchi method, enabling a systematic evaluation of each factor's effect on motor performance. In defining the optimization characteristics, torque ripple, back-EMF, and line voltage were treated as "smaller-the-better" characteristics, aiming to minimize electromagnetic fluctuation and excessive voltage. In contrast, efficiency was set as a "larger-the-better" characteristic, aiming to improve energy conversion performance. The signal-to-noise (SN) ratio response graph and ANOVA were calculated for each performance parameter—

Table 6
Control factors and their level settings.

Factor	Symbol	Level 1	Level 2	Level 3
Slot opening width	A	2.15 mm	2.35 mm	2.55 mm
Air gap	B	0.38 mm	0.48 mm	0.58 mm
Magnet expansion angle	C	130°	140°	150°
Wire diameter	D	0.50 mm	0.55 mm	0.60 mm
Magnet thickness	E	1.2 mm	1.4 mm	1.6 mm
Number of turns	F	30 turns	35 turns	40 turns

torque ripple, back-EMF, line voltage, and efficiency—to determine the contribution and significance of each design factor and to identify the optimal parameter combination. Finally, the optimized design results were compared with the initial configuration to verify the effectiveness and improvement achieved through the optimization process.

The SN ratio response graph for the torque ripple under the "smaller-the-better" criterion is shown in Fig. 5. Since this characteristic aims to minimize torque ripple, a larger SN ratio indicates a smaller and more stable torque ripple. As illustrated in Fig. 5, the optimal combination for minimizing torque ripple is $A_1B_3C_1D_1E_1F_3$. The corresponding ANOVA results are summarized in Table 7, which shows that the magnet expansion angle has the most significant effect on torque ripple, with a variance ratio of 27.12 and a contribution of 55.95%. The number of turns and the air gap are the most important factors, with a variance ratio of 10.75 and a combined contribution of 20.9%.

Using the same methodology, we selected the S/N ratio response criterion for both back-EMF and line voltage as the "smaller-the-better" characteristic. The corresponding ANOVA results for back-EMF and line voltage are summarized in Tables 8 and 9, respectively. As shown in Table 8, magnet thickness is the most influential factor affecting back-EMF, with a variance ratio of 50.10% and a contribution of 73.71%, demonstrating its dominant impact on this performance parameter. The next most significant factors are the slot opening width and the air gap, each exhibiting a variance ratio of 14.20% and a contribution of 14.20%. Table 9 indicates that the number of turns (Factor F) is the dominant factor affecting the line voltage, with a variance ratio of 92.03% and a contribution of 85.8%, highlighting its critical role in reducing back-EMF and maintaining voltage stability. The remaining factors (A, B, C, D, and E) each contribute less than 10%, suggesting that they function primarily as secondary or fine-tuning parameters in the optimization process. Following the line voltage analysis, motor efficiency was optimized using a "larger-the-better" S/N ratio. As shown in Table 10, ANOVA results indicate that Factor D is the dominant parameter, with a variance ratio of 61.12% and a contribution of 72.16%. Factor C has a moderate effect (11.72%), whereas Factors A and B have minor effects and Factors E and F are negligible. The low total error contribution (9.28%) confirms the stability and reliability of the model.

Since these optimal configurations differ among performance objectives, a multi-objective compromise analysis was conducted using the overall balance method (OBM) of the Taguchi approach to achieve balanced optimization across all characteristics. On the basis of the integrated results summarized in Table 11, the optimal levels of each factor were compared, with

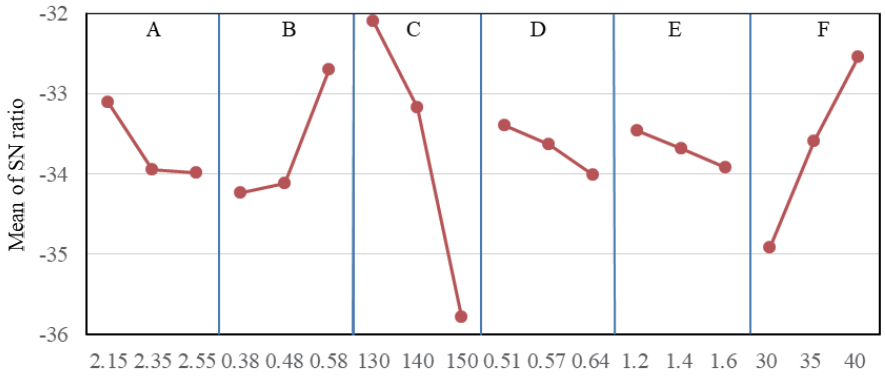

Fig. 5. (Color online) SN ratio response graph for torque ripple (smaller-the-better characteristic).

Table 7
ANOVA for torque ripple.

Factor	Sum of Squares	DOF	Variance	Pure sum of squares	F-ratio	Contribution (%)
A	4.42	2	6.64	10.92	5.61	9.87
B	13.29	2	32.14	10.92	27.12	55.95
C	64.28	2	32.14	61.91	27.12	55.95
D	1.75	2	12.75	23.12	10.75	20.90
E	0.95	2	—	—	—	—
F	25.49	2	12.75	23.12	10.75	20.90
Error	0.47	—	—	—	—	—
Total error	7.11	6	1.19	14.70	—	13.28

Table 8
ANOVA for back-EMF (smaller-the-better characteristic).

Factor	Sum of squares	DOF	Variance	Pure sum of squares	F-ratio	Contribution (%)
A	0.10	2	2.94	5.31	10.46	14.20
B	5.88	2	2.94	5.31	10.46	14.20
C	1.31	2	—	—	—	—
D	0.00	2	—	—	—	—
E	1.96	2	14.07	27.58	50.10	73.71
F	28.14	2	—	—	—	—
Error (e)	0.03	—	—	—	—	—
Total error (eT)	3.37	8	0.28	4.52	—	12.08
Total (T)	37.41	12	—	37.41	—	100

Table 9
ANOVA for line voltage (smaller-the-better characteristic).

Factor	Sum of squares	DOF	Variance	Pure sum of squares	F-ratio	Contribution (%)
A	0.17	2	1.80	3.18	8.66	7.22
B	3.60	2	1.80	3.18	8.66	7.22
C	0.60	2	0.30	0.36	2.14	1.07
D	0.89	2	0.44	0.47	2.14	1.07
E	0.48	2	0.24	0.60	2.76	1.42
F	38.24	2	19.12	37.82	92.03	85.80
Error (e)	1.25	6	0.21	2.60	—	5.91
Total error (eT)	44.09	12	—	44.09	—	100

Table 10
ANOVA for efficiency (larger-the-better characteristic).

Factor	Sum of squares	DOF	Variance	Pure sum of squares	F-ratio	Contribution (%)
A	0.01	2	0.07	0.12	6.70	6.80
B	0.14	2	0.07	0.12	6.70	6.80
C	0.23	2	0.12	0.21	10.77	11.72
D	1.31	2	0.65	1.28	61.12	72.16
E	0.04	2	—	—	—	—
F	0.01	2	—	—	—	—
Error (e)	0.06	6	0.01	0.17	—	9.28
Total error (eT)	1.78	12	—	1.78	—	100

Table 11
OBM analysis.

Factor	Slot opening	Air gap	Magnet arc angle	Wire diameter	Magnet thickness	Number of turns
Torque Ripple	1	3	1*	1	1	3*
Back-EMF	3*	3*	3	3	1*	1
Line Voltage	3	3*	3	1	1	1
Efficiency	1	3	3	3*	3	3*
Overall Balance	3	3	1	3	3	1

the most influential factors marked with an asterisk. After evaluating the trade-offs among the four performance indicators—torque ripple, back-EMF, line voltage, and efficiency—the final optimal parameter combination was determined to be $A_3B_3C_1D_3E_1F_1$. The final optimized design parameters are as follows: slot opening = 2.55 mm, air gap = 0.58 mm, magnet arc angle = 130°, wire diameter = 0.6 mm, magnet thickness = 1.2 mm, and number of turns = 30.

3.3 Optimization results and discussion

For an operating condition of 1000 rpm, Table 12 shows the back-EMF and cogging torque peak values of the 8-pole/12-slot motor before and after optimization. As shown in the table, the RMS phase voltage decreased from 5.78 to 2.39 V, representing a reduction of approximately 58.7%, while the cogging torque peak decreased from 0.08 to 0.01 N·m, resulting in an 87.5% improvement. These results demonstrate that the proposed optimization design effectively reduces both back-EMF and cogging torque, thereby enhancing the motor's operational smoothness and stability.

For identical operating conditions (current: 1.35 A; speed: 2678.5 rpm), Table 13 shows the simulation results of the 8-pole/12-slot motor before and after optimization. The RMS line voltage decreased from 36.12 to 13.93 V, representing a 61.4% reduction; the efficiency improved from 77.3 to 82.1%, an increase of approximately 6.2%; and the torque ripple dropped significantly from 109.9 to 45.6%, representing a 58.5% decrease. These results clearly demonstrate that the Taguchi-based parameter optimization led to substantial overall performance improvement, particularly in reducing voltage demand and torque fluctuation.

Table 12
Back-EMF and cogging torque before and after optimization.

Model	Cogging torque	Back-EMF
Initial model	0.08 N·m	5.78 V
Optimized model	0.01 N·m	2.39 V
Improvement	↓ 87.5%	↓ 58.7%

Table 13
Motor performance before and after optimization.

Parameter	Line voltage	E. power	M. power	Torque	Efficiency	Torque ripple
Before optimization	36.12 V	75.82 W	58.63 W	0.21 N·m	77.3%	109.9%
After optimization	13.93 V	27.93 W	22.93 W	0.08 N·m	82.1%	45.6%
Change trend	↓ 61.4%	↓ 63.16%	↓ 60.89%	↓ 61.9%	↑ 6.2%	↓ 58.5%

4. Experimental Results

To ensure consistency between the design parameters and the actual performance, the optimized motor was physically assembled and experimentally verified against the simulation results. Before winding, an insulation frame was mounted on the stator to prevent friction between the copper wires and the stator slot edges. This friction can otherwise damage the insulation layer or cause short circuits, thereby affecting efficiency and reliability. The insulation frame was first modeled in 3D in SolidWorks and fabricated via photopolymerization-based 3D printing. To enhance winding stability and accuracy, the upper section of the insulation frame was designed with raised positioning structures that assist in wire fixation and tension control during winding, ensuring uniform wire alignment and stress distribution. The complete exploded structure is shown in Fig. 6(a), while the assembled stator with the insulation frame is illustrated in Fig. 6(b). For the winding process, the optimized motor used a manual CW approach with a 0.6-mm-diameter enameled wire, with 30 turns per slot to maintain the designed coil density and slot fill factor. The completed winding appearance is shown in Fig. 6(c). To ensure reliable electrical connections, the neutral junctions and phase leads of the three-phase windings were soldered with tin and reinforced using heat-shrink tubing to improve insulation and mechanical strength. After soldering, the line-to-line resistance of the three phases was measured to be 1.2 Ω for each phase, with negligible deviation, indicating uniform winding quality and a stable manufacturing process that provides a reliable foundation for subsequent performance testing and validation.

Under a motor speed condition of 2265 rpm, the back-EMF waveform was analyzed. The experimental results were compared with the simulated waveforms obtained from Flux2D, as shown in Fig. 7. The results indicate that the measured waveform closely matches the overall trend of the simulated waveform, demonstrating good accuracy in the model construction and parameter configuration. However, the measured voltage peak is slightly lower than the simulated value, with a deviation of approximately 9%. This discrepancy is presumed to result mainly from variations in environmental conditions during fabrication and nonuniformities introduced by manual winding. These include inconsistencies in coil tension and winding

(a) (b) (c)

Fig. 6. (Color online) Stator fabrication: (a) exploded structural view, (b) completed stator structure, and (c) completed stator winding.

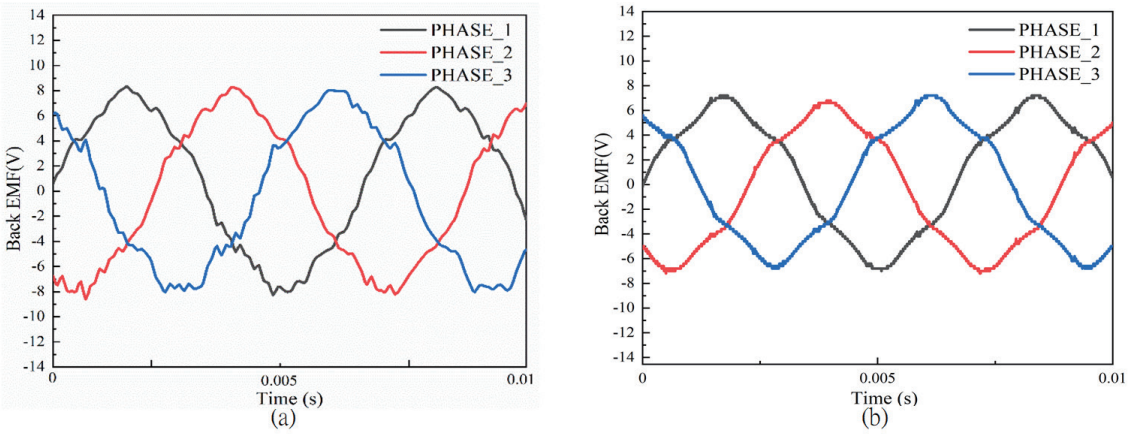

Fig. 7. (Color online) Motor back-EMF waveforms: (a) experimental measurement and (b) simulation analysis.

density, which cause minor differences in the actual magnetic field distribution compared with the simulation model. Overall, the experimental results show strong agreement with the simulation predictions, confirming the correctness and reliability of the finite element model established in this study.

Table 14 shows the experimental and Flux2D simulation results for the 8-pole/12-slot motor under high-speed operating conditions. The measured speed reached 3024 rpm, which is 4.8% lower than the simulated 3178 rpm, primarily because of bearing friction and aerodynamic drag. The measured torque was 0.15 N·m versus a simulated value of 0.16 N·m, corresponding to a 6.3% deviation, indicating good predictive capability of the simulation model. The electrical power exhibited a 5.7% difference (68.67 W measured vs 72.82 W simulated), mainly caused by contact resistance and winding temperature rise. Mechanical power showed the largest deviation at 11.4% (47.82 W vs 53.99 W), consistent with frictional and viscous losses encountered during

Table 14
Experimental and simulation results of the 8-pole/12-slot motor.

Item	Speed (rpm)	Torque (N·m)	Electrical power (W)	Mechanical power (W)	Efficiency (%)
Experiment	3024	0.15	68.67	47.82	70.0
Simulation	3178	0.16	72.82	53.99	74.1

physical operation. Consequently, the measured efficiency of 70% was slightly lower than the simulated 74.1%, representing a 4.1% reduction attributable to real-world mechanical losses and additional contact resistance. Overall, the simulation results correlate well with experimental observations, demonstrating that the Flux2D model can effectively estimate motor performance under high-speed conditions with acceptable accuracy. Overall, the experimental and simulation results show strong agreement, with deviations remaining within acceptable limits. The observed differences are mainly associated with nonuniform winding, manufacturing tolerances, and environmental factors during testing. These findings confirm that the developed simulation model accurately represents the motor's operating behavior and can reliably predict electromagnetic performance and efficiency under high-speed conditions.

5. Conclusions

In this study, we systematically investigated the effects of motor geometric parameters on torque ripple and back-EMF using FluxMotor and Flux2D finite-element simulations, combined with sensitivity analysis and the Taguchi optimization method. Six critical factors—magnet expansion angle, air gap, number of turns, slot opening width, enameled wire diameter, and magnet thickness—were identified as dominant contributors to motor performance. Optimization results demonstrate that adjusting these parameters significantly reduces torque ripple, back-EMF, and line voltage, while improving overall efficiency. For the optimized 8-pole/12-slot motor, the back-EMF RMS decreased by 58.7% and the cogging torque by 87.5% at 1000 rpm. At the operating point of 1.35 A and 2678.5 rpm, line voltage was reduced by 61.4%, efficiency improved by 6.2%, and torque ripple decreased by 58.5%. Compared with the reference motor, the optimized design achieved an efficiency gain of 22.53%, with a speed increase of nearly 500 rpm under identical load conditions. Experimental validation further confirmed consistency with simulation, showing only minor deviations due to manual winding and environmental factors.

Beyond performance enhancement, in this work, we introduced a practical and industry-oriented novelty by conducting multi-objective electromagnetic optimization under strict commercial product constraints. Unlike many existing studies that optimize BLDC motors without considering mechanical compatibility, the proposed design strictly preserves the original casing dimensions of a commercial dual-fan motor, enabling direct replacement without structural modification. In addition, the rotor configuration was innovatively modified from a conventional ring-type magnet to a segmented tile-type magnet arrangement, achieving a substantial 62.98% reduction in magnet material usage while maintaining electromagnetic performance. This design not only reduces material cost but also enhances mechanical reliability under high-speed operation.

Overall, the proposed optimization framework integrates FEA, sensitivity analysis, and Taguchi-based parameter optimization into a manufacturable and cost-effective design methodology. The demonstrated improvements in performance, material utilization, and industrial applicability highlight the technical and economic novelty of this work, providing a practical and scalable design reference for next-generation high-efficiency BLDC motors. Future research may incorporate automated winding processes to further minimize manufacturing-induced deviations and explore additional design dimensions, such as alternative slot-to-pole combinations, magnet mounting strategies, core fixation techniques, and coating processes, to further enhance efficiency and reliability.

Acknowledgments

We would like to thank the National Science Council, Taiwan, for financially supporting this research under grant no. NSTC 114-2637-E-230-001.

References

1 D. Xu, M. Lin, X. Fu, L. Hao, W. Zhang, and N. Li: IEEE Trans. Appl. Supercond. **26** (2106) 1. https://doi.org/10.1109/TASC.2016.2519524
2 C. Y. He and T. Wu: Energies **11** (2018) 1360. https://doi.org/10.3390/en11061360
3 A. Siadatan, M. Roohisankestani, and S. Farhangian: Proc. Int. Symp. Power Electronics, Electrical Drives, Automation and Motion (IEEE, 2018) 353−358. https://doi.org/10.1109/SPEEDAM.2018.8445245
4 I. W. Lan and H. W. Ho: Proc. Int. Conf. Electrical and Electronic Technologies for Automotive (IEEE, 2018) 1–5. https://doi.org/10.23919/EETA.2018.8493159
5 H. J. Lee, J. H. Kim, J. Lee, S. J. Joo, and C. E. Kim: Proc. 21st Int. Conf. Electrical Machines and Systems (IEEE, 2018) 329−331. https://doi.org/10.23919/ICEMS.2018.8549113
6 M.-H. Lin, C.-C. Yang, B.-W. Huang, J.-Y. Lin, and C.-Y. Chen: Int. J. Eng. Technol. Innovation **15** (2024) 44. https://doi.org/10.46604/ijeti.2024.13595
7 S. Shastri, U. Sharma, and B. Singh: Proc. 2020 IEEE Int. Conf. Power Electronics, Drives and Energy Systems (IEEE, 2020) 1−6. https://doi.org/10.1109/PEDES49360.2020.9379863
8 O. Iegorov, O. Iegorova, M. Kundenko, and N. Potryvaieva: Proc. 2020 IEEE Problems of Automated Electrodrive Theory and Practice (IEEE, 2020) 1−4. https://doi.org/10.1109/PAEP49887.2020.9240820
9 S. Leitner, H. Gruebler, and A. Muetze: Proc. 2020 IEEE Applied Power Electronics Conf. and Exposition (IEEE, 2020) 279−284. https://doi.org/10.1109/APEC39645.2020.9124114
10 S. Chakraborty, J. V. Singh, and K. Hatua: Proc. 2022 IEEE Int. Conf. Power Electronics, Smart Grid, and Renewable Energy (IEEE, 2022) 1−6. https://doi.org/10.1109/PESGRE52268.2022.9715864
11 M. Dragos and A. Maricel: Proc. 2023 10th Int. Conf. Modern Power Systems (IEEE, 2023) 1−9. https://doi.org/10.1109/MPS58874.2023.10187580
12 A. M. Ajamloo, A. Ghaheri, and E. Afjei: Proc. 2019 10th Int. Power Electronics, Drive Systems and Technologies Conf. (IEEE, 2019) 34−39. https://doi.org/10.1109/PEDSTC.2019.8697586
13 U. Sharma and B. Singh: IEEE Trans. Ind. Appl. **57** (2021) 3562. https://doi.org/10.1109/TIA.2021.3072020
14 F. Mahmouditabar, M. G. Gorji, and A. Vahedi: Proc. 2021 12th Power Electronics, Drive Systems, and Technologies Conf. (IEEE, 2021) 1−4. https://doi.org/10.1109/PEDSTC52094.2021.9405939
15 J. Cao, X. He, D. Li, B. Jia, and Q. Liu: Proc. 2023 IEEE 6th Int. Electrical and Energy Conf. (IEEE, 2023) 4110−4114. https://doi.org/10.1109/CIEEC58067.2023.10166646
16 B080 Dual blower: https://www.powercircling.com/product/2/60/27
17 J. F. Gieras: Permanent Magnet Motor Technology: Design and Applications (CRC Press, Boca Raton, 2009) 3th ed., Chap. 6.
18 S. I. Suriano-Sánchez, M. Ponce-Silva, V. H. Olivares-Peregrino, and S. E. De León-Aldaco: Eng **3** (2022) 646. https://doi.org/10.3390/eng3040044
19 J. Qi, Z.-Q. Zhu, G. W. Jewell, L. Yan, C. Gan, Y. Ren, S. Brockway, and C. Hilton: IET Electr. Power Appl. **17** (2023) 628. https://doi.org/10.1049/elp2.12293
20 W. Hao, G. Zhang, W. Liu, H. Liu, and Y. Wang: Energies **16** (2023) 422. https://doi.org/10.3390/en16010422
21 H.-I. Park and M.-M. Koo: J. Magn. **30** (2025) 395. https://doi.org/10.4283/JMAG.2025.30.3.395